Research Article | Open Access

Microstructures

Yu et al. Microstructures 2026, 6, 20260129 DOI:10.20517/microstructures.2026.235

High-entropy and grain boundary engineering for enhanced energy storage performance in $Bi_{0.5}Na_{0.5}TiO_3$-based ceramics

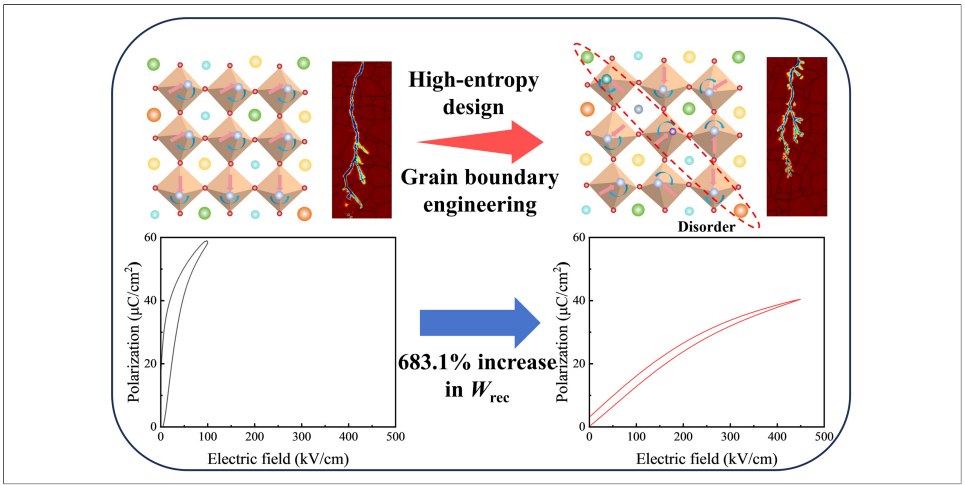
Chongwen Yu[1], Dong-Xu Li[1], Zhenxiang Wang[1], Wenli Liu[1], You Zhang[1,2], Qi Zhou[1], Zhipeng Xu[1], Rui Qiu[1], Zong-Yang Shen[1]

Keywords:
Energy storage ceramics, high-entropy, grain boundary engineering, $Bi_{0.5}Na_{0.5}TiO_3$, moderate electric fields

Citation: Yu, C.; Li, D. X.; Wang, Z.; Liu, W.; Zhang, Y.; Zhou, Q.; Xu, Z.; Qiu, R.; Shen, Z. Y. High-entropy and grain boundary engineering for enhanced energy storage performance in $Bi_{0.5}Na_{0.5}TiO_3$-based ceramics. *Microstructures* **2026**, *6*, 20260129. https://dx.doi.org/10.20517/microstructures.2026.235

Received: 19 Aug 2026 **First Decision:** 9 Sep 2026 **Revised:** 17 Sep 2026 **Accepted:** 30 Sep 2026 **Published:** 15 Oct 2026

Academic Editor: Dawei Wang **Copy Editor:** Fangling Lan **Production Editor:** Fangling Lan



Abstract

High-entropy (HE) design has enabled ultrahigh energy storage performance (ESP) in lead-free dielectric ceramics. However, this is achieved almost exclusively under very high electric fields above 500 kV/cm. In the practically relevant moderate electric-field range of 200-500 kV/cm, the unavoidable tradeoff between the breakdown strength (E_b) and polarization difference (ΔP) restricts the attainable ESP and hampers industrial applications. Herein, we apply HE grain boundary engineering to fabricate (1-x)$(Bi_{0.5}Na_{0.5})_{0.7}(Ba_{0.3}Sr_{0.7})_{0.3}TiO_3$-$xLa(Mg_{2/3}Nb_{1/3})O_3$ (BNBST-xLMN) ceramics to overcome this limitation. The incorporation of LMN increases the configurational entropy and induces phase competition. Phase-field simulations are used to quickly identify that the x = 0.08 model has a low remnant polarization (P_r) and high maximum polarization (P_{max}) under normalized electric fields. Atomic-scale observations reveal that short-range polar and long-range nonpolar regions coexist, along with randomly tilted oxygen octahedra in the BNBST-0.08LMN ceramic, effectively reducing polarization anisotropy while maintaining

[1]Jiangxi Key Laboratory of Advanced Ceramic Materials, China National Light Industry Key Laboratory of Functional Ceramic Materials, School of Materials Science and Engineering, Jingdezhen Ceramic University, Jingdezhen 333403, Jiangxi, China.
[2]Decorative Materials R&D Center, Ceramic Research Institute of Light Industry of China, Jingdezhen 333403, Jiangxi, China.

Correspondence to: Dr. Zong-Yang Shen, Jiangxi Key Laboratory of Advanced Ceramic Materials, China National Light Industry Key Laboratory of Functional Ceramic Materials, School of Materials Science and Engineering, Jingdezhen Ceramic University, Jingdezhen 333403, Jiangxi, China. E-mail: shenzongyang@jcu.edu.cn

strong local dipole correlations. Additionally, the Mg oxide compounds are observed within the grain boundaries and serve as pinning centers that refine the grain size, improve insulation performance, and retard the propagation of electrical trees. As a result, the BNBST-0.08LMN ceramic achieves a recoverable energy density (W_{rec}) of 6.50 J/cm^3 together with a high efficiency (η) of 86.42% at 450 kV/cm. The material also shows a stable ESP and fast charge-discharge performance ($t_{0.9} \approx 45$ ns). Therefore, this study provides both a general route to achieving improved ESP in $Bi_{0.5}Na_{0.5}TiO_3$-based ceramics at moderate electric fields and a promising candidate for integrated industrial power systems.

INTRODUCTION

For pulsed-power applications, dielectric capacitors stand out among energy-storage devices because they charge and discharge extremely quickly, deliver high power densities, and withstand repeated operation over long lifetimes[1-4]. The energy storage performance (ESP) of a dielectric for this purpose is usually evaluated via its recoverable energy density (W_{rec}) and storage efficiency (η). Both quantities are obtained from the polarization-electric field (P-E) loops through[4,5]:

$$W_{tot} = \int_0^{P_{max}} E \, dP \tag{1}$$

$$W_{rec} = \int_{P_r}^{P_{max}} E \, dP \tag{2}$$

$$\eta = W_{rec}/W_{tot} \times 100\% \tag{3}$$

where P, P_r, P_{max}, and E denote the electric polarization, remnant polarization, maximum polarization, and externally applied electric field, respectively. Optimizing the ESP therefore requires a simultaneous increase in P_{max} and breakdown strength (E_b) together with a suppressed P_r and reduced hysteresis-related energy dissipation. Lead-based antiferroelectrics are attractive in this respect because their double hysteresis loops afford excellent ESP[6-8], but the toxicity of Pb^{2+} restricts their use. Among lead-free candidates, $Bi_{0.5}Na_{0.5}TiO_3$-based (BNT) ceramics are particularly promising because the strong covalent Bi^{3+}-O^{2-} hybridization (6*s*-2*p* orbitals) yields a high P_{max}[9-12]. However, their ESP is limited by a low E_b of roughly 100 kV/cm and by large hysteresis losses that originate from long-range-ordered ferroelectric domains[13].

Numerous strategies have been pursued to improve the ESP of BNT-based ceramics, including optimized sintering[14,15], core-shell structuring[16-18], complex-ion substitution[9,19,20], defect engineering[21,22], domain control[23-25] and, more recently, the high-entropy (HE) strategy[26,27]. Of these, HE design has proven particularly effective in tailoring P_r[28]. By definition, an HE ceramic is a single-phase solid solution with more than five principal cations, each with an atomic fraction of 5-35 at%, and a configurational entropy (S_{config}) exceeding 1.5 R, where R is the gas constant. The S_{config} value is evaluated via[29]

$$S_{config} = -R\left[\left(\sum_{i=1}^{N} x_i \ln x_i\right)_{A\text{-site}} + \left(\sum_{j=1}^{M} x_j \ln x_j\right)_{B\text{-site}}\right] \tag{4}$$

where N (M) and x_i (x_j) represent the total number of atomic species and their corresponding atomic fractions, respectively. Although the HE strategy has recently produced remarkably high energy storage densities, they have largely been obtained under very high applied electric fields above 500 kV/cm[13,30-32]. Operating capacitors under such extreme conditions is hazardous for both equipment and personnel and

compromises their long-term reliability. Therefore, this critical limitation underscores the need for advanced dielectric materials capable of exhibiting high W_{rec} values within a moderate electric field range of 200-500 kV/cm[33-35]. The HE strategy typically results in refinement of the grain size due to structural disorder, and P_r is minimized through disruption of the long-range ordered ferroelectric domain[36,37]. Although a smaller grain size could enhance E_b, ε_r and P_{max} decrease accordingly[30,38]. Owing to this intrinsic tradeoff between E_b and ΔP (P_{max}-P_r) in the HE strategy, achieving a high W_{rec} value under moderate electric fields remains challenging.

Double perovskite $La(Mg_{2/3}Nb_{1/3})O_3$ (LMN) contains complex ions (La^{3+}, Mg^{2+}, and Nb^{5+}), which have emerged as a promising modifier for optimizing the ESP of lead-free ceramics[39-41]. Substituting complex ions increases entropy, induces an inhomogeneous structure, and reduces polarization anisotropy, thereby minimizing hysteresis losses. Although researchers have claimed that introducing LMN can refine grain size and enhance E_b by increasing entropy, the doping of Mg^{2+} ions promotes sintering and increases grain size[42,43]. Therefore, the relationship between LMN introduction and grain-size evolution remains unclear. It is difficult to explain the enhancement in E_b solely via grain size. Furthermore, traditional methods typically require extensive experimentation to determine the optimal entropy range when developing high-ESP HE materials. This requires significant time and resources and limits the realization and optimization of these materials. Recently, phase-field simulations have been demonstrated to intuitively reproduce entropy-controlled domain evolution and polarization reversal at the nanoscale[23,27,44-46], thus overcoming the limitations of traditional experimental methods. This method allows the rapid identification of the optimal LMN content by identifying the entropy regions corresponding to low P_r and high P_{max} values via phase-field simulation. Additionally, because P_{max} and P_r depend on polarization switching and response behavior, the local domain structure must be investigated after introducing LMN.

Our previous studies reported a novel BNT-based ceramic, designated as $(Bi_{0.5}Na_{0.5})_{0.7}(Ba_{0.3}Sr_{0.7})_{0.3}TiO_3$ (BNBST)[47,48], which is a medium-entropy ceramic with S_{config} = 1.27 R that reaches a P_{max} near 50 μC/cm² at a low E_b of ~100 kV/cm. However, this system exhibits a relatively large P_r of ~15 μC/cm² together with strong hysteresis losses. In this study, LMN is introduced as a modifier to fabricate BNBST-xLMN ceramics to further enhance the ESP of BNBST ceramics under moderate electric fields. The introduction of LMN increases the configurational entropy of this system, leading to structural disorder. Phase-field simulations are used to quickly identify that the x = 0.08 model (S_{config} = 1.78 R) has rapid and reversible polarization responses, along with a high P_{max} under normalized electric fields [Figure 1A]. Experimentally, the optimized BNBST-0.08LMN ceramic attains an excellent W_{rec} of 6.50 J/cm³ with η = 86.42% at 450 kV/cm. In addition, the Rietveld refinement indicates that introducing LMN triggers phase competition, thereby widening the temperature coefficient of capacitance (TCC). The local domain structure of the BNBST-0.08LMN ceramic demonstrates short-range polar regions dispersed in the long-range nonpolar region, with the random tilting of an oxygen octahedron, which effectively minimizes the polarization anisotropy and maintains strong local dipole correlations. In addition, the grain size first decreases, then increases, and finally decreases again as x increases, and the BNBST-0.08LMN sample exhibits a medium grain size of ~1.23 μm. In particular, Mg oxide is observed at the grain boundaries of the BNBST-0.08LMN ceramic, which enhances the insulation performance of this system and slows the electric tree propagation with multiple bifurcating propagation paths [Figure 1B]. This confirms that the enhanced E_b is related not only to grain-size refinement but also to the Mg oxide compound located within the grain boundaries. In addition, the ESP of the BNBST-0.08LMN ceramic remains robust under various environmental conditions, and its ultrafast discharge time of 45 ns underlines its suitability for pulsed-power systems. Overall, this study demonstrates the use of HE and grain-boundary engineering to achieve a high ESP under moderate electric fields.

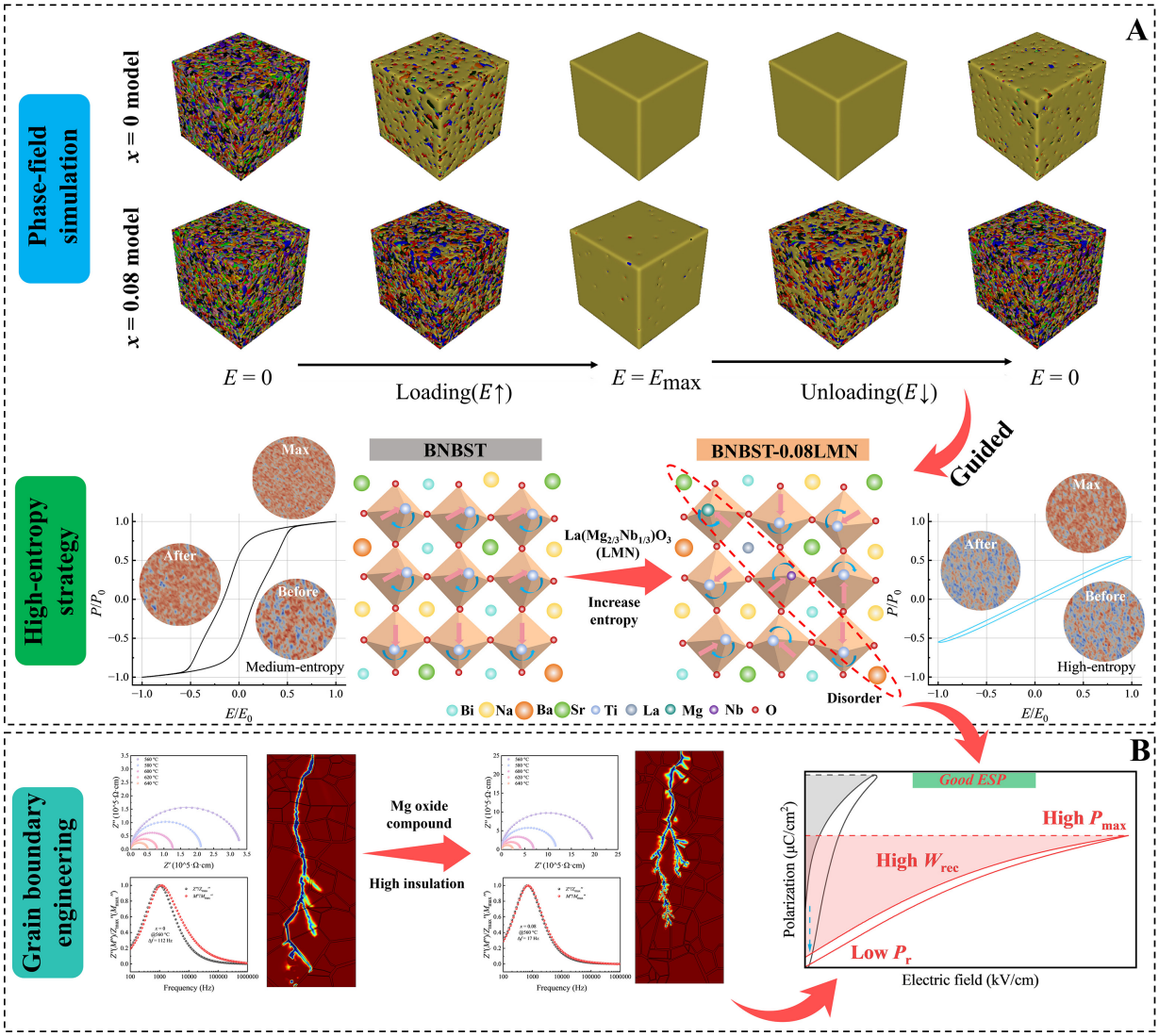


Figure 1. Schematic of the optimization of the ESP in BNBST ceramics via (A) the phase-field simulation-guided high-entropy strategy and (B) grain boundary engineering.

MATERIALS AND METHODS

Sample synthesis

Ceramics with the nominal composition of (1-x)($Bi_{0.5}Na_{0.5}$)$_{0.7}$($Ba_{0.3}Sr_{0.7}$)$_{0.3}TiO_3$-xLa($Mg_{2/3}Nb_{1/3}$)O_3, hereafter referred to as BNBST-xLMN, were prepared using a conventional solid-state route. The modifier content x was varied from 0 to 0.10 in increments of 0.02. The starting oxides and carbonates, including Nb_2O_5 (99.9%), MgO (99.9%), La_2O_3 (99.9%), $BaCO_3$ (99.9%), $SrCO_3$ (99.9%), TiO_2 (98.0%), Na_2CO_3 (99.9%) and Bi_2O_3 (99.9%), were all obtained from a commercial supplier (Sinopharm Chemical Reagent Co. Ltd., Shanghai, China). Each reagent was used in the amount required by the nominal stoichiometry using the purities to correct the batch weights, and the batch was then ball-milled for 24 h in a planetary mill. After drying, the mixtures were calcined at 850 °C for 3 h, milled a second time for 24 h, and granulated with a 5 wt% polyvinyl alcohol solution. The granulated powder was pressed into green disks that were 13 mm in diameter and approximately 1 mm thick under a uniaxial pressure of 120 ± 10 MPa. Binder burnout was performed at 650 °C for 3 h, after which the disks were sintered in air at 1,220-1,240 °C for 2 h.

Structural characterization

Phase identification was conducted via X-ray diffraction (XRD; SMARTLAB, Japan) using Cu Kα radiation, and local vibrational features were probed using a Raman spectrometer (in Via, Renishaw, UK). The surface morphologies were examined using scanning electron microscopy (SEM; JSM-6700F, JEOL, Japan). Specimens for transmission electron microscopy (TEM) were cut using a dual-beam focused ion beam workstation (Helios 5 UC, ThermoFisher Scientific, USA). Microstructure and selected-area electron diffraction (SAED) data were recorded using a field-emission TEM (Talos F200X, ThermoFisher Scientific, USA) operated at 200 kV, and the elemental distributions were mapped using the energy-dispersive X-ray spectroscopy detector of the Cs-corrected microscope (Super-X, ThermoFisher Scientific, USA). Atomic-resolution imaging and compositional analysis were performed using double spherical-aberration-corrected scanning TEM (STEM; Spectra 300, ThermoFisher Scientific, USA) with probe- and image-side correctors at 300 kV. Cation positions in the STEM images were refined by two-dimensional Gaussian fitting, and the polarization vectors, magnitudes, and angles were extracted using custom MATLAB routines. Polarization magnitudes above 50 pm were automatically discarded, and all angles were normalized into the 0°-360° range. Ultraviolet-visible (UV-Vis) absorbance spectra were recorded on a UV3600 Plus spectrophotometer (Shimadzu, Japan) using specimens polished to 0.20 mm thickness over a transmission window of 300-700 nm.

Electrical property measurements

The dielectric spectra as a function of temperature were acquired using a precision impedance analyzer (HP4294A, Agilent, USA) between -90 and 400 °C. Complex impedance tests were conducted at 560, 580, 600, 620, and 640 °C using a precision impedance analyzer (HP4294A, Agilent, USA). For ferroelectric testing, the thickness of the specimens was polished to ~100 ± 5 μm and coated with Au to form electrodes with an area of 0.00785 cm^2. Charge-discharge samples were thinned to the same thickness of ~100 ± 5 μm and printed using a central circular Ag electrode (2 mm in diameter), which was fired at 650 °C for 40 min. The dynamic polarization response was probed by piezoresponse force microscopy (PFM; Jupiter XR, Oxford Instruments, USA) at various fields and relaxation periods. Polarization-electric field (*P*-*E*) loops were recorded at 10 Hz on a ferroelectric analyzer (Trek model 609B) wired in the standard Sawyer-Tower configuration, and the frequency-, temperature-, and cycle-dependent loops were collected on a ferroelectric workstation. The temperature-dependent charge-discharge behavior was evaluated using a custom resistor-inductor-capacitor circuit (CFD-003, Tongguo Technology, China) placed inside a temperature-controlled chamber.

Phase-field simulations

Domain evolution in the BNBST-*x*LMN ceramics was modeled with a phase-field approach in which the local polarization vector $P = (P_1, P_2, P_3)$ describes the domain pattern. The temporal development of P was obtained by solving the time-dependent Ginzburg-Landau equation together with the mechanical and electrical equilibrium conditions for the displacement and electric displacement fields[49]:

$$\frac{\partial P_i}{\partial t} = -L\frac{\delta F}{\delta P_i} + E_i^{\text{thermal}} \tag{5}$$

$$\frac{\partial}{\partial x_j}\left(\sigma_{ij}(r,t)\right) = 0 \tag{6}$$

$$\nabla \cdot D = \rho_f \tag{7}$$

In Eq. (5), L is a kinetic coefficient associated with domain-wall mobility and F is the total free energy; σ_{ij}, ρ_f, r, and t denote the stress tensor, free-charge density, spatial coordinate, and time, respectively. For a bulk

system, the total free energy can be calculated using

$$\begin{aligned} F &= F_{\text{bulk}}(\boldsymbol{P}) + F_{\text{grad}}(\boldsymbol{P}) + F_{\text{elastic}}(\boldsymbol{P}) + F_{\text{elec}}(\boldsymbol{P},\boldsymbol{E}) \\ &= \int_V \left(f_{\text{bulk}} + f_{\text{grad}} + f_{\text{elastic}} + f_{\text{elec}}\right) dV \end{aligned} \tag{8}$$

where the four contributions $F_{\text{bulk}}(\boldsymbol{P})$, $F_{\text{grad}}(\boldsymbol{P})$, $F_{\text{elastic}}(\boldsymbol{P})$ and $F_{\text{elec}}(\boldsymbol{P},\boldsymbol{E})$ are the bulk, domain-wall (gradient), elastic, and electrostatic energies, respectively; f_{bulk}, f_{grad}, f_{elastic}, and f_{elec} are the corresponding densities; and E is the applied static field. The bulk term may be expanded to the sixth order in the polarization:

$$\begin{aligned} f_{\text{bulk}} &= \alpha_1\left(P_1^2+P_2^2+P_3^2\right)+\alpha_{11}\left(P_1^4+P_2^4+P_3^4\right) \\ &+\alpha_{12}\left(P_1^2P_2^2+P_1^2P_3^2+P_2^2P_3^2\right)+\alpha_{111}\left(P_1^6+P_2^6+P_3^6\right) \\ &+\alpha_{112}\left[P_1^4\left(P_2^2+P_3^2\right)+P_3^4\left(P_2^2+P_1^2\right)+P_2^4\left(P_3^2+P_1^2\right)\right]+\alpha_{123}P_1^2P_2^2P_3^2 \end{aligned} \tag{9}$$

where α_i, α_{ij}, and α_{ijk} are the Landau coefficients. The elastic energy density is $f_{\text{elastic}} = 1/2c_{ijkl}(\varepsilon_{ij} - \varepsilon_{ij}^0)(\varepsilon_{kl} - \varepsilon_{kl}^0)$, where c_{ijkl}, ε_{ij}, and ε_{ij}^0 are the elastic stiffness, total strain, and eigenstrain, respectively; the eigenstrain is related to the polarization through $\varepsilon_{ij}^0 = Q_{ijkl}P_kP_l$ where Q_{ijkl} represents the electrostrictive coefficients. The gradient term $f_{\text{grad}} = 1/2G_{ijkl}P_{i,j}P_{k,l}$ involves the gradient coefficients G_{ijkl}, and the electrostatic contribution is $f_{\text{elec}} = -P_i(r)(E_i(r) - 1/2P_i(r)E_i^{\text{in}}(r))$, where $E_i(r)$ is the applied field and $E_i^{\text{in}}(r)$ is the field generated by the dipoles themselves.

The simulations were performed on a 64 × 64 × 64 grid with 1 nm spacing in each direction. The Landau parameters of the $(Bi_{0.5}Na_{0.5})_{0.7}(Ba_{0.3}Sr_{0.7})_{0.3}TiO_3$ host were $\alpha_1 = -1.725770 \times 10^8$ m²·N/C², $\alpha_{11} = -9.200542 \times 10^7$ m⁶·N/C⁴, $\alpha_{12} = 3.213195 \times 10^8$ m⁶·N/C⁴, $\alpha_{111} = 1.947874 \times 10^8$ m¹⁰·N/C⁶, $\alpha_{112} = 1.015568 \times 10^9$ m¹⁰·N/C⁶, $\alpha_{123} = -6.963512 \times 10^9$ m¹⁰·N/C⁶, $Q_{11} = 0.070$ m⁴/C², $Q_{12} = -0.020$ m⁴/C², $Q_{44} = 0.0775$ m⁴/C², $c_{11} = 1.746 \times 10^{11}$ N/m², $c_{12} = 7.937 \times 10^{10}$ N/m², and $c_{44} = 1.11 \times 10^{11}$ N/m². To mimic the experimental conditions, a Gaussian-distributed electric field was superimposed, whose width scales with the entropy-dependent diffusion-doping level. The field has a zero mean and a standard deviation of x MV/cm, where x follows the configurational entropy.

COMSOL simulation

Finite-element modeling (COMSOL) was used to map the spatial distributions of the electric potential and local field and thereby assess the field homogeneity in the ceramics. A rectangular two-dimensional geometry of 12.00 μm × 4.63 μm was built, and the grain-boundary thickness was kept identical in all models so that the effect of grain size could be directly compared. The grain/grain-boundary networks were constructed from the SEM images of the $x = 0$ and 0.08 samples. Dielectric constants assigned to the grains and boundaries were derived from the average grain size together with the overall permittivity measured at 1 kHz, while the breakdown parameters were taken from the impedance results. An external voltage was applied by fixing the electric potential at the upper edge of the model and grounding the lower edge, with periodic boundary conditions on the lateral sides. The electrostatic equations were then solved to obtain the equilibrium potential and field distributions.

RESULTS AND DISCUSSION

Microstructural and polarization switching behavior analysis

Figure 2A shows the XRD patterns of all samples, collected between $2\theta = 20°$ and 80°. The pure BNBST ceramic shows the (001) and (100) diffraction peaks from 22° to 23° [Figure 2A1]. This indicates that the pure BNBST ceramic is mainly composed of the tetragonal (*P4bm*) phase. As x increases, the (001) and (100) diffraction peaks merge into a single (100) peak, indicating that BNBST-*x*LMN ceramics gradually transition

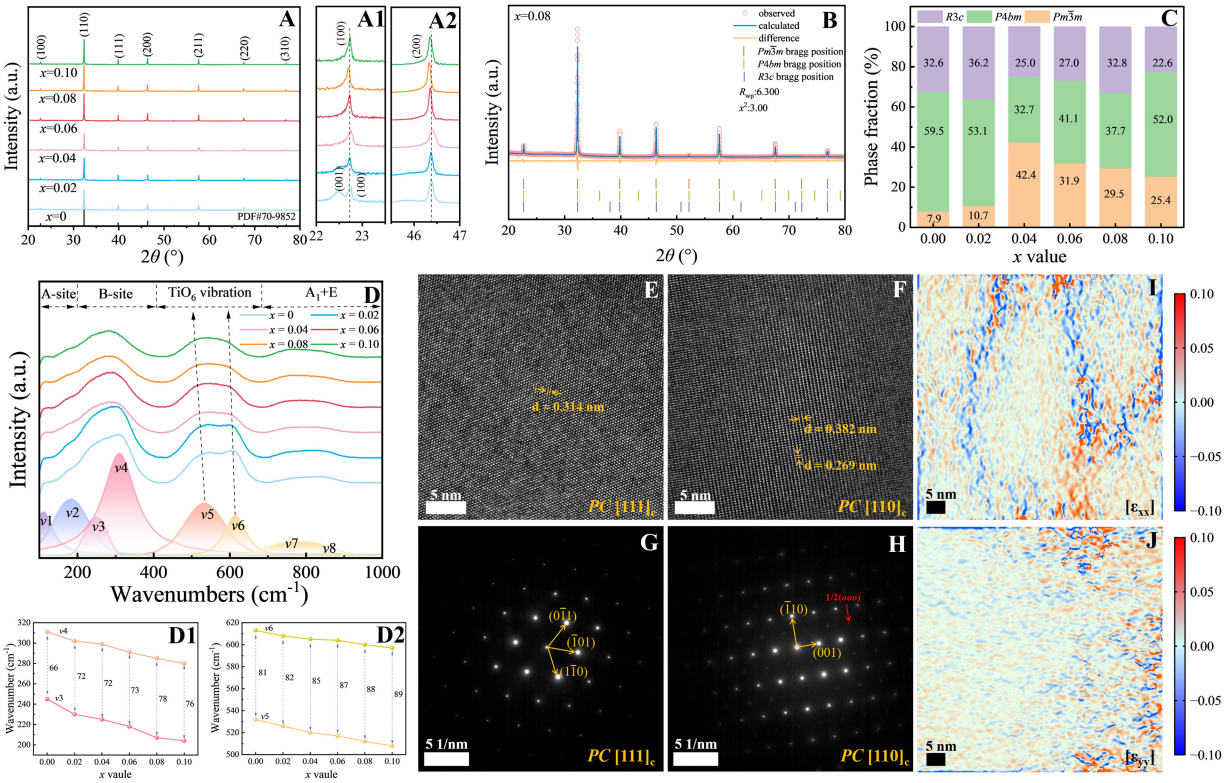


Figure 2. Structural characterization of the BNBST-*x*LMN ceramics. (A) XRD patterns of all compositions, with enlarged views shown in (A1) 22°-23.5° and (A2) 45.5°-47°. (B) Rietveld refinement of the x = 0.08 ceramic. (C) Fraction evolution of different phases versus the x value. (D) Raman spectra of all samples and their Lorentzian deconvolution results. Wavenumber shifts of the (D1) $v3$/$v4$ and (D2) $v5$/$v6$ phonon modes versus the x value. HR-TEM images of the x = 0.08 ceramic along the (E) $[111]_c$ and (F) $[110]_c$ axes. SAED patterns along the (G) $[111]_c$ and (H) $[110]_c$ axes. GPA results showing the (I) $[\varepsilon_{xx}]$ and (J) $[\varepsilon_{yy}]$ strain directions for the x = 0.08 ceramic.

to a pseudo-cubic (*PC*)-phase. Additionally, the (200) diffraction peak simultaneously migrates to smaller angles [Figure 2A2], which is consistent with lattice expansion as the La^{3+} radius (1.36 Å, CN = 12) is close to that of the A-site Bi^{3+} (1.38 Å, CN = 12), whereas the average $(Mg_{2/3}Nb_{1/3})^{3+}$ radius (0.69 Å, CN = 6) exceeds that of the B-site Ti^{4+} (0.61 Å, CN = 6)[50]. Additionally, with increasing x value to 0.10, the tolerance factor (t) exhibits a progressive reduction from 0.9731 to 0.9584, while the configuration entropy (S_{config}) increases from 1.27 to 1.86 R [Supplementary Figure 1]. In perovskites, the oxygen octahedral tilting is governed by t, which is known to construct polar phases such as the rhombohedral *R*3*c* and tetragonal *P*4*bm*[30]. As established in the literature, oxygen octahedra maintain a regular undistorted geometry when t > 0.9850, while tilting occurs as t decreases below this critical value[51]. To quantitatively analyze the phase fractions and competition behavior induced by LMN modification, XRD Rietveld refinements were carried out on all BNBST-*x*LMN ceramics. A three-phase model incorporating cubic *Pm*$\bar{3}$*m*, tetragonal *P*4*bm*, and rhombohedral *R*3*c* phases was employed for the Rietveld refinement process[52]. The goodness-of-fit indicators, including the chi-square distribution (Chi^2) and *R*-weighted pattern (R_{wp}), for the optimal BNBST-0.08LMN ceramic are presented in Figure 2B. All refinement results are statistically valid, as the R_{wp} values for all samples are consistently below the 10% threshold [Supplementary Figure 2]. The evolution of phase fractions with increasing x value is plotted in Figure 2C, providing clear evidence of complex phase competition in the BNBST-*x*LMN ceramics. When x = 0.04, the ceramic transforms from medium-entropy to high-entropy, which exhibits the highest *Pm*$\bar{3}$*m* fraction. When x > 0.04, the *Pm*$\bar{3}$*m* fraction decreases, and the x = 0.08 ceramic exhibits a relatively higher *P*4*bm* fraction with similar *Pm*$\bar{3}$*m* and *R*3*c* fractions.

To gain deeper insight into the local structural changes induced by LMN modification, Raman spectroscopy measurements were performed on all BNBST-*x*LMN ceramics, and the resulting spectra are presented in Figure 2D. Each Raman spectrum was deconvoluted into eight distinct peaks using Peakfit software, which can be grouped into four characteristic regions based on their corresponding vibrational modes[53]: (1) the low-frequency region (< 200 cm^{-1}) containing *v*1 and *v*2 modes, which are characteristic of A-site ion translational vibrations; (2) the mid-low frequency region (200-400 cm^{-1}) comprising *v*3 and *v*4 modes, associated with B-O bond stretching vibrations; (3) the mid-high frequency region (400-700 cm^{-1}) with *v*5 and *v*6 modes, corresponding to oxygen octahedral tilting and bending motions; and (4) the high-frequency region (> 700 cm^{-1}) featuring *v*7 and *v*8 modes, arising from the superposition of A1 LO and E LO modes. A gradual red shift of the *v*3 and *v*4 modes to lower wavenumbers is observed with increasing *x* values, providing direct spectroscopic evidence for weakened B-O bond strength and elongated B-O interatomic distances [Figure 2D1]. Additionally, the progressive increase in peak separation between *v*3 and *v*4 results in a significantly broadened and flattened spectral profile. This same evolution behavior is observed for the *v*5 and *v*6 modes in the mid-high frequency range [Figure 2D2]. The observed spectral broadening and flattening directly result from the elevated S_{config} in the HE system, which introduces substantial lattice disordering and creates spatially varying local electric fields, thereby destabilizing long-range ferroelectric domains and favoring the formation of polar nanoregions (PNRs).

To clarify the microstructure at the nanoscale, high-resolution TEM (HR-TEM) imaging was performed on the $x = 0.08$ ceramic along the $[111]_c$ and $[110]_c$ zone axes [Figure 2E and F], and the corresponding SAED patterns are shown in Figure 2G and H, respectively. The $[110]_c$ pattern contains clear 1/2(*ooo*) superlattice spots that arise from antiphase $a^-a^-a^-$ tilting of the oxygen octahedra (i.e., the *R*3*c* phase[25]), while the 1/2(*ooe*) superlattice spots from in-phase $a^0a^0c^+$ tilting (a *P*4*bm* signature) appear in Supplementary Figure 3[54]. The simultaneous observation of both superlattice spots confirms that antiphase and in-phase octahedral tilts coexist, indicating multiphase coexistence. Moreover, geometric phase analysis (GPA) conducted along the $[110]_c$ zone axis [Figure 2I and J] reveals disordered lattice spacing and localized strain, as evidenced by the alternating red and blue color mapping. Therefore, the introduction of LMN increases S_{config}, enhances lattice distortion, and eliminates the long-range ferroelectric order.

The atomic-scale structure of the $x = 0.08$ ceramic was examined by aberration-corrected STEM along the $[110]_c$ zone axis, and the high-angle annular dark-field (HAADF) image is shown in Figure 3A. Moreover, the polarization vectors (yellow arrows) were derived from the displacement of B-site cations relative to the surrounding A-site cations. Based on 2D Gaussian peak fitting, displacement vectors pointing along $[001]_c$ were related to the tetragonal phase (*T*-phase, blue area), those along $[111]_c$ to the rhombohedral phase (*R*-phase, pink area), and displacements below 4 pm to the *PC*-phase, yellow area, corresponding to weak polar or nonpolar regions. The spatial angle and displacement magnitude distributions are presented in Figure 3B and C, respectively. The local structure of the $x = 0.08$ ceramic exhibits the coexistence of *R*-*T*-*PC* tri-phases, wherein the short-range *T*- and *R*-phases are randomly dispersed within the long-range *PC*-phase. This indicates that short-range polar and long-range nonpolar regions coexist, thereby reducing hysteresis losses while maintaining strong local dipole correlations. Notably, diffuse transition regions (purple area) between different phase domains [Figure 3A], which act as low-energy pathways for polarization rotation and significantly reduce polarization anisotropy. Quantitative analysis of the B-site ion displacements [Figure 3D] shows a slight preferential orientation toward the *T*-phase direction, which correlates well with the phase fraction results obtained from the Rietveld refinement. The average displacement of B-site ions was measured to be 4.69 pm [Figure 3E], which is smaller than that in typical ferroelectric materials, further confirming the weakened long-range polar component. To directly visualize oxygen octahedral tilting, STEM-annular bright-field (ABF) imaging was performed along the $[110]_c$ zone axis [Figure 3F], enabling clear visualization of oxygen atoms and illustrating the octahedral tilt of ABO_3 perovskite. A magnified view

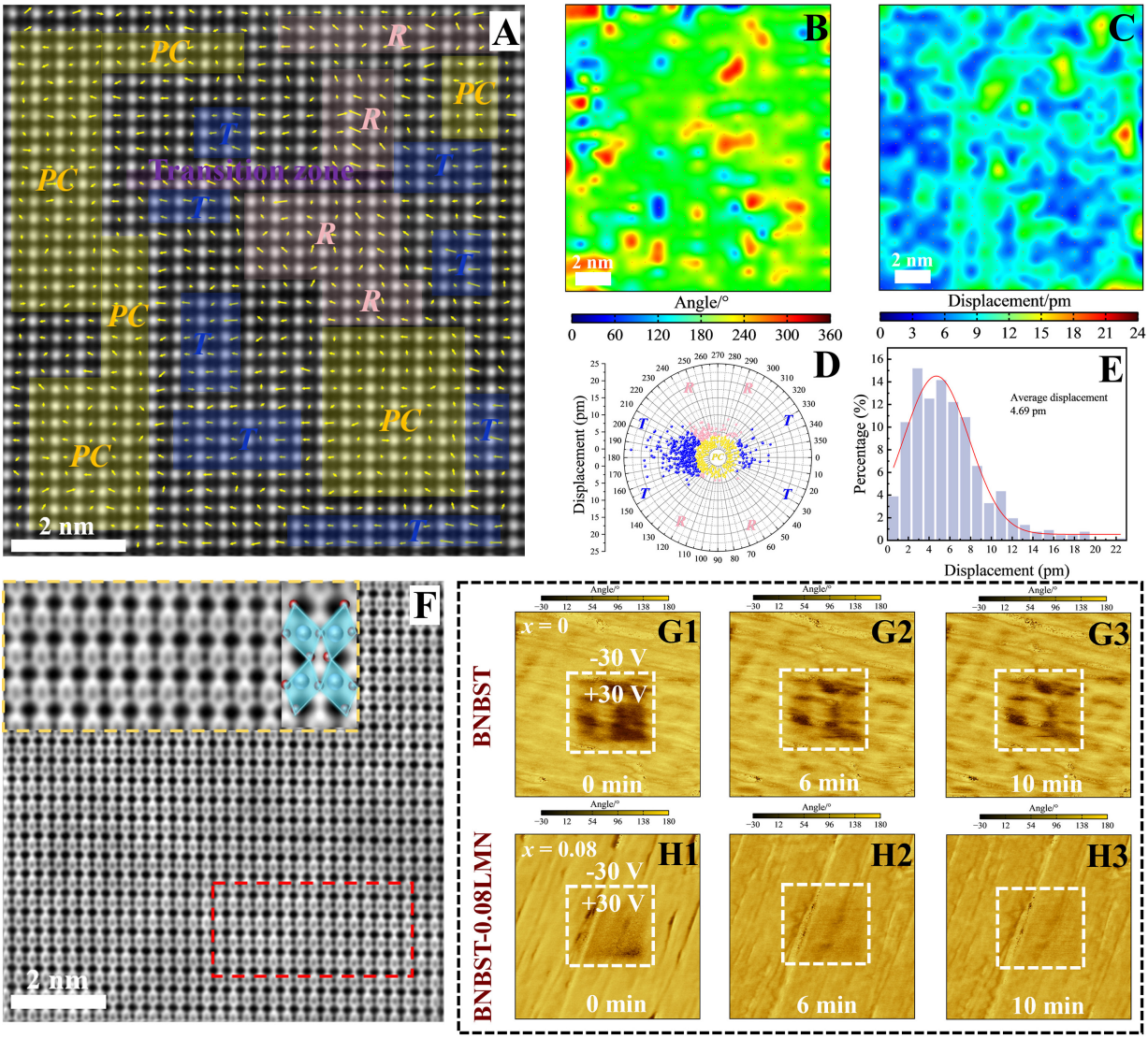


Figure 3. Atomic-scale local structure and dynamic polarization behavior of the x = 0.08 ceramic. (A) Local polarization structure derived from a STEM-HAADF image, showing B-site ion displacement vectors along the $[110]_c$ zone axis. (B) Polarization angle and (C) polarization magnitude maps. (D) Polarization projections of B-site cation displacements and (E) statistical distribution of polarization magnitudes. (F) STEM-ABF image obtained along the $[110]_c$ direction; the inset highlights the oxygen octahedral tilting. PFM time-dependent phase images of the (G1-G3) x = 0 and (H1-H3) x = 0.08 ceramics.

of the red-framed area in Figure 3F (shown in the yellow frame) further elucidates this octahedral tilting, with B-site cations located near the oxygen atoms within the yellow-shaded region. These observations, combined with the statistical oxygen octahedral tilt angle analysis in Supplementary Figure 4, demonstrate that the HE strategy induces random oxygen octahedral tilting. This tilting generates local random elastic and electric fields, which effectively pin domain walls and moderate the polarization reorientation dynamics of this system.

To further elucidate the correlation between the dynamic polarization response and local structural features under an applied electric field, PFM testing was conducted on the x = 0 and 0.08 ceramics. The PFM measurement protocol involved applying a negative DC voltage to a 5 μm × 5 μm area using a conductive tip, followed by a positive DC voltage of equal magnitude to the central 2 μm × 2 μm region. Phase images of pure BNBST captured in the out-of-plane mode at various relaxation times are shown in Figure 3G1-G3.

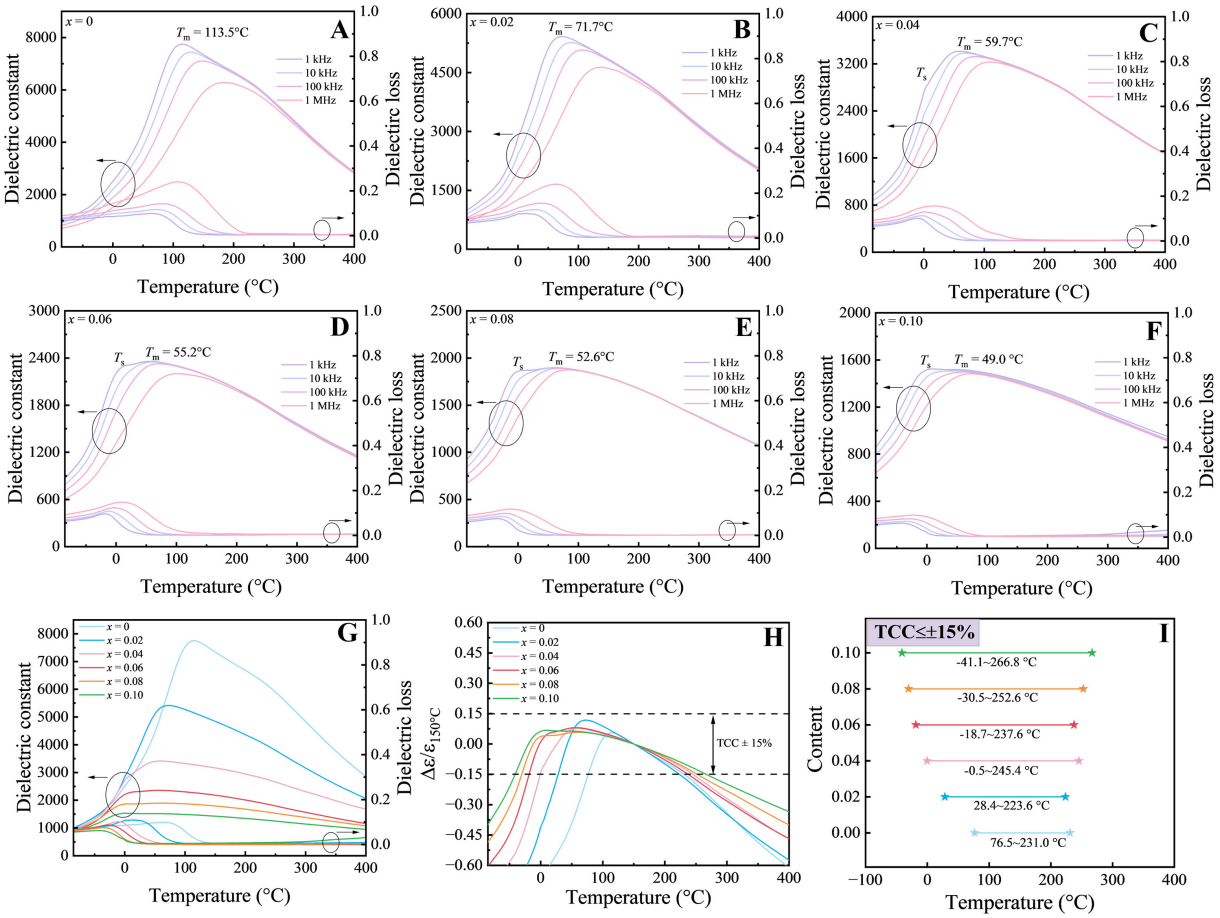


Figure 4. (A-F) Temperature-dependent dielectric spectra at various frequencies for all samples. (G) Comparison of the dielectric-temperature curves for all samples at 1 kHz. (H) TCC curves and (I) temperature windows in which TCC remains within ±15%.

When subjected to 30 V, the BNBST ceramic exhibits a nearly 180° polarization reversal; however, a significant fraction of the switched domains remains in their reversed states even after 10 min of relaxation. This demonstrates that the polarization switching is slow and largely irreversible, which relates to the strong hysteresis losses. By contrast, the BNBST-0.08LMN ceramic demonstrates a highly dispersed, punctate polarization switching pattern at 30 V, where most domains swiftly recover their original orientations within 10 min of voltage removal [Figure 3H1-H3]. This fast, reversible switching stems from highly dynamic PNRs with minimized polarization anisotropy, which is consistent with the previous phase-field results and local structural analysis.

Energy storage performance analysis

The temperature dependence of the dielectric properties was measured at different frequencies for all samples [Figure 4A-F], and the 1 kHz curves are overlaid in Figure 4G for direct comparison. A clear frequency dispersion is observed with increasing x value, accompanied by a downward shift of the temperature of the permittivity maximum (T_m). In particular, a thermal evolution peak (T_s) appears at low temperatures when $x \geq 0.04$ and is attributed to the temperature-driven phase transition. This observation demonstrates that the competing phases not only transform due to the introduction of LMN, but also interconvert as the temperature increases. This dynamic phase competition effectively broadens and flattens the dielectric constant peak.

The temperature stability for capacitor applications was evaluated through the TCC, calculated by[55]

$$TCC = \frac{\varepsilon - \varepsilon_R}{\varepsilon_R} \times 100\% \quad (10)$$

where ε is the permittivity at the measurement temperature, and ε_R is the permittivity at the reference temperature of 150 °C, which corresponds to the operation temperature for automotive engine-compartment electronics and industrial switching power supplies. All samples satisfy the Electronic Industries Alliance requirement of TCC within ±15% over a certain temperature window [Figure 4H]. The BNBST-0.08LMN ceramic keeps TCC within ±15% from -30.5 to 252.6 °C [Figure 4I], a markedly broader range than that of pure BNBST.

The ferroelectric and energy-storage behavior was characterized through bipolar *P*-*E* hysteresis loops [Figure 5A] and the corresponding current-electric field (*I*-*E*) curves [Figure 5B]. The pure BNBST ceramic shows a high P_{max} and a large P_r value because its polarization switching is irreversible, and the associated sluggish response generates pronounced current peaks in the *I*-*E* curves. As x increases, the loops become progressively slimmer, P_r markedly decreases, and the current peaks flatten, indicating that the high S_{config} and dynamic PNRs delay polarization saturation and suppress hysteresis loss. Figure 5C presents the unipolar loops of the BNBST-0.08LMN ceramic under different electric fields. At 450 kV/cm, this ceramic combines a low P_r of 3.20 μC/cm² with a high P_{max} of 40.43 μC/cm² and strongly reduced hysteresis compared with pure BNBST, owing to the HE strategy and the simultaneous presence of short-range polar and long-range nonpolar regions. Furthermore, E_b values were repeatedly measured, and the measurement reliability was assessed via the Weibull statistical analysis using[56]:

$$X_i = \ln(E_i) \quad (11)$$

$$Y_i = \ln(\ln(1/(1 - i/(n + 1)))) \quad (12)$$

where E_i is the breakdown strength of the i-th measurement and n is the total number of tests. Additionally, X_i and Y_i denote the transformed horizontal and vertical coordinates of the Weibull plot, respectively. The Weibull shape parameter β, which indicates the dispersion of the breakdown strength data, is greater than 10 for all samples [Figure 5D], indicating good measurement reliability and uniform sample quality. Notably, Eb progressively increases with increasing x and reaches a maximum at $x = 0.08$; the underlying mechanisms for this enhancement will be discussed later. Figure 5E depicts the electric field dependence evolution of W_{rec} and η of the BNBST-xLMN ceramics, and Figure 5F compares the W_{rec} and η values at their respective E_b values. Under these conditions, pure BNBST exhibits W_{rec} = 0.83 J/cm³ with η = 44.45% at 100 kV/cm, whereas BNBST-0.08LMN achieves W_{rec} = 6.50 J/cm³ with η = 86.42% at 450 kV/cm. These values correspond to relative increases of approximately 683.1% in W_{rec} and 94.4% in η [Figure 5G]. A comprehensive comparison with recent studies of lead-free energy storage ceramics demonstrates that the BNBST-0.08LMN ceramic achieves excellent ESP under moderate electric fields [Supplementary Table 1, Figure 5H], making it highly attractive for next-generation compact and integrated power electronic systems.

SEM analysis was performed on all samples to elucidate the mechanism of the improved E_b in the BNBST-xLMN ceramics. The surface morphologies of the BNBST-xLMN ceramics without any additional processing are shown in Figure 6A-F. The pure BNBST ceramic has an average grain size of 1.36 μm, and a small number of pores are visible in the cross-sectional micrograph [Supplementary Figure 5A]. The average grain size of BNBST-0.02LMN ceramic is smaller than that of pure BNBST, which is due to the increased S_{config} value. However, for $0.06 \geq x \geq 0.04$, the average grain size increases. This seems contradictory to the grain refinement commonly observed in the HE strategy. In addition, the average grain size decreases when

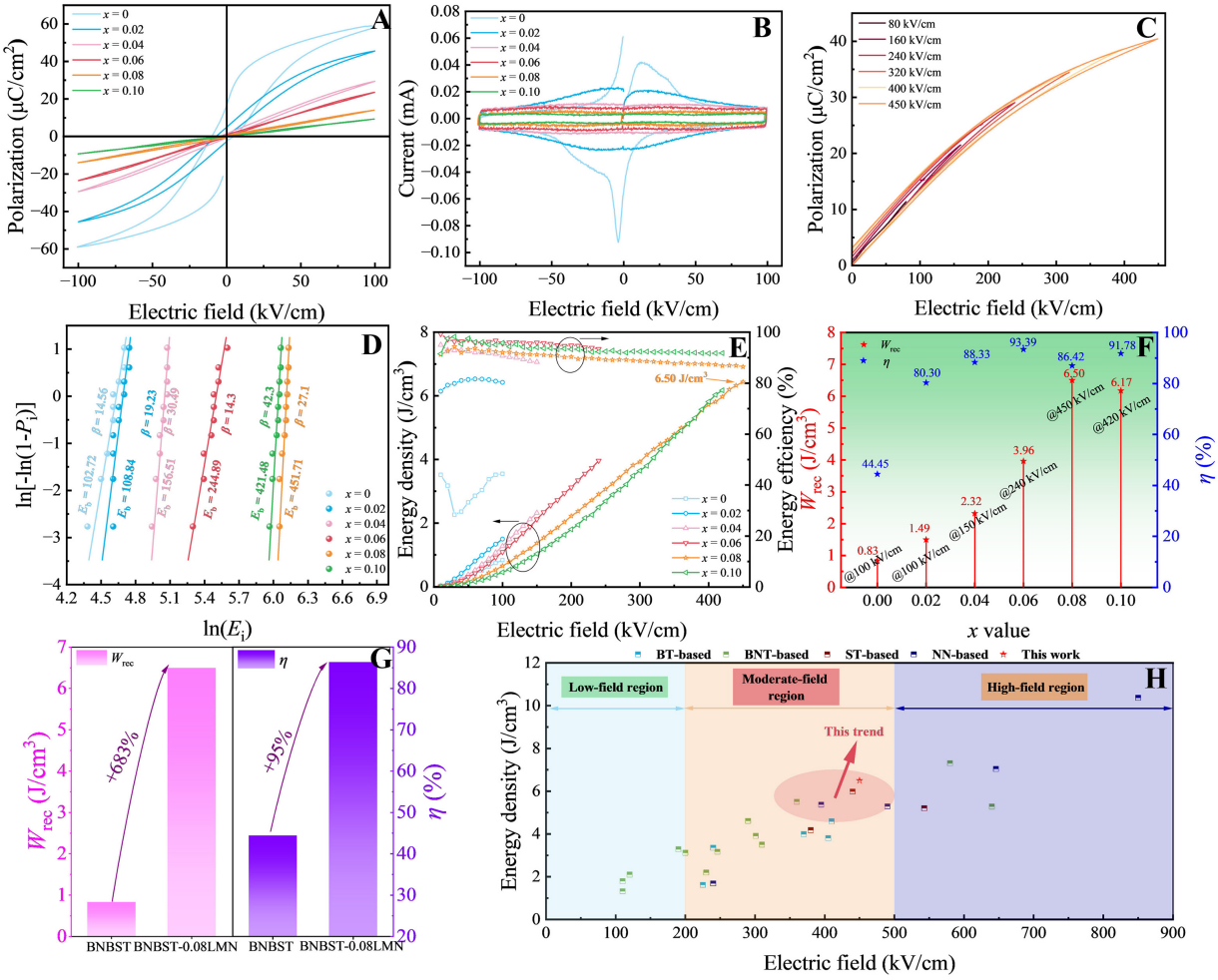


Figure 5. (A) Bipolar *P-E* loops and (B) corresponding *I-E* curves at 100 kV/cm for all samples. (C) Unipolar *P-E* loops for the x = 0.08 ceramic under different electric fields. (D) Weibull distribution of E_b for all samples. (E) W_{rec} and η for all samples versus the applied electric field. (F) W_{rec} and η values at the E_b value for each sample. (G) Comparison of W_{rec} and η between the x = 0 and 0.08 ceramics at their respective E_b values. (H) W_{rec}-E_b comparison with recently reported lead-free ceramics (references listed in Supplementary Table 1).

$x \geq 0.08$, and the BNBST-0.08LMN ceramic shows a smaller average grain size (≈ 1.23 μm) than the pure BNBST ceramic, with reduced pore structures in the cross-section [Supplementary Figure 5B]. Moreover, Mg oxide compounds (such as MgO and $MgTiO_3$) are observed at the grain boundaries [Figure 6G-K]. At moderate x values (such as 0.04 and 0.06), Mg^{2+} ions enter the lattice, lowering the strain energy barrier.

$$\Delta G_{strain} = 4\pi M N_A \left[\frac{r_0}{2(r_d - r_0)^2} + \frac{1}{3(r_d - r_0)^3} \right],$$

where M is Young's modulus, N_A is the Avogadro constant, r_0 is the ionic radius of the host lattice site, and r_d is the ionic radius of the dopant. This occurs because the radius (r_d) of the dopant ions is larger than that (r_0) of the substituted ions[57]. This lower energy barrier enhances the mass transport kinetics across grain boundaries during sintering, leading to more pronounced grain growth, which also conceals the effect of the HE strategy on grain refinement. When $x \geq 0.08$, some Mg^{2+} ions start to segregate and form Mg oxide compounds at the grain boundaries. These compounds act as pinning centers, hindering grain boundary motion and inhibiting further grain growth. Therefore, the average grain size is related not only to the HE strategy, but also to the existence of the Mg oxide compounds at the grain boundaries.

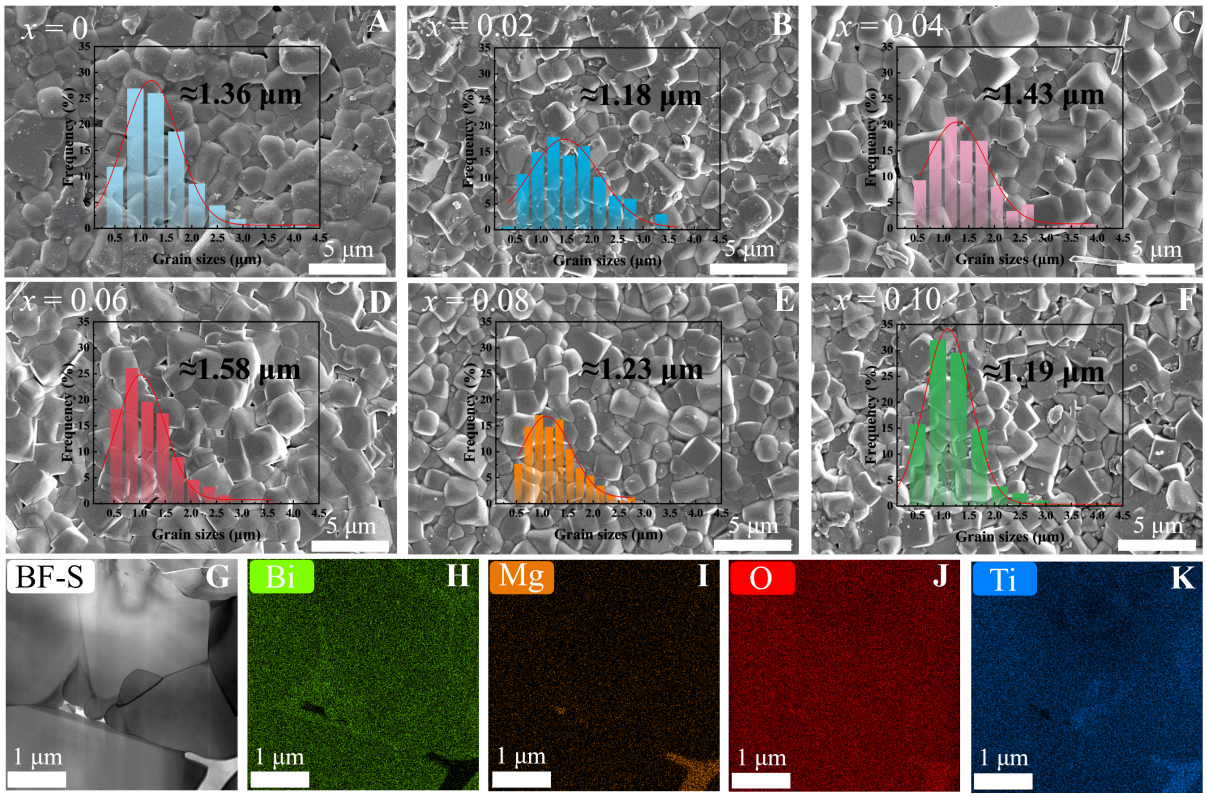


Figure 6. (A-F) Surface SEM micrographs and grain size distributions for all samples. (G) Bright-field TEM image of the x = 0.08 ceramic together with the (H) Bi, (I) Mg, (J) O, and (K) Ti elemental maps.

In addition to the grain size, the impedance characteristics and electrical homogeneity between grains and grain boundaries also affect E_b. To clarify these factors, complex impedance spectroscopy measurements were conducted on the BNBST-xLMN ceramics [Figure 7A and B, Supplementary Figure 6]. All Nyquist plots exhibit depressed semicircular arcs rather than perfect semicircles, which is a typical signature of non-Debye relaxation behavior. Notably, the radius of the impedance semicircular arc monotonically increases with x up to x = 0.08, indicating a progressive enhancement in the insulating resistance of the ceramics. The BNBST-0.08LMN ceramic demonstrates the best insulation performance, with the largest semicircular arc radius. However, the insulation performance slightly decreases at x = 0.10. This means that an excess of Mg oxide compounds at the grain boundaries can lead to deterioration. To further analyze the electrical homogeneity, the frequency positions of the imaginary impedance (Z″) and imaginary modulus (M″) peaks were compared. For pure BNBST, these peaks are separated by 112 Hz [Figure 7C], signaling strong electrical heterogeneity. By contrast, the BNBST-0.08LMN ceramic shows nearly overlapping Z″ and M″ peaks with a frequency difference of only 17 Hz [Figure 7D], indicating improved electrical homogeneity[58,59].

A major source of electrical inhomogeneity is Maxwell-Wagner interfacial polarization, which is caused by the permittivity and conductivity mismatch between grains and boundaries. The resulting space charge accumulation at the interfaces enhances the local field and lowers E_b. To quantify this, the impedance data were fitted with a dual resistor-constant phase element equivalent circuit that separates the contributions of each component. The degree of electrical heterogeneity can be quantified using the activation energy difference considering the insulation performances of the grains and grain boundaries ($\Delta\Phi = |E_\text{Þ} - E_{GB}|$), which is directly proportional to the strength of Maxwell-Wagner interfacial polarization[54]. A decrease in $\Delta\Phi$ suppresses space charge buildup at grain-grain boundary interfaces, thus making a smaller $\Delta\Phi$ beneficial for enhancing E_b. The activation energies for grains ($E_\text{Þ}$) and grain boundaries (E_{GB}) were calculated by fitting the

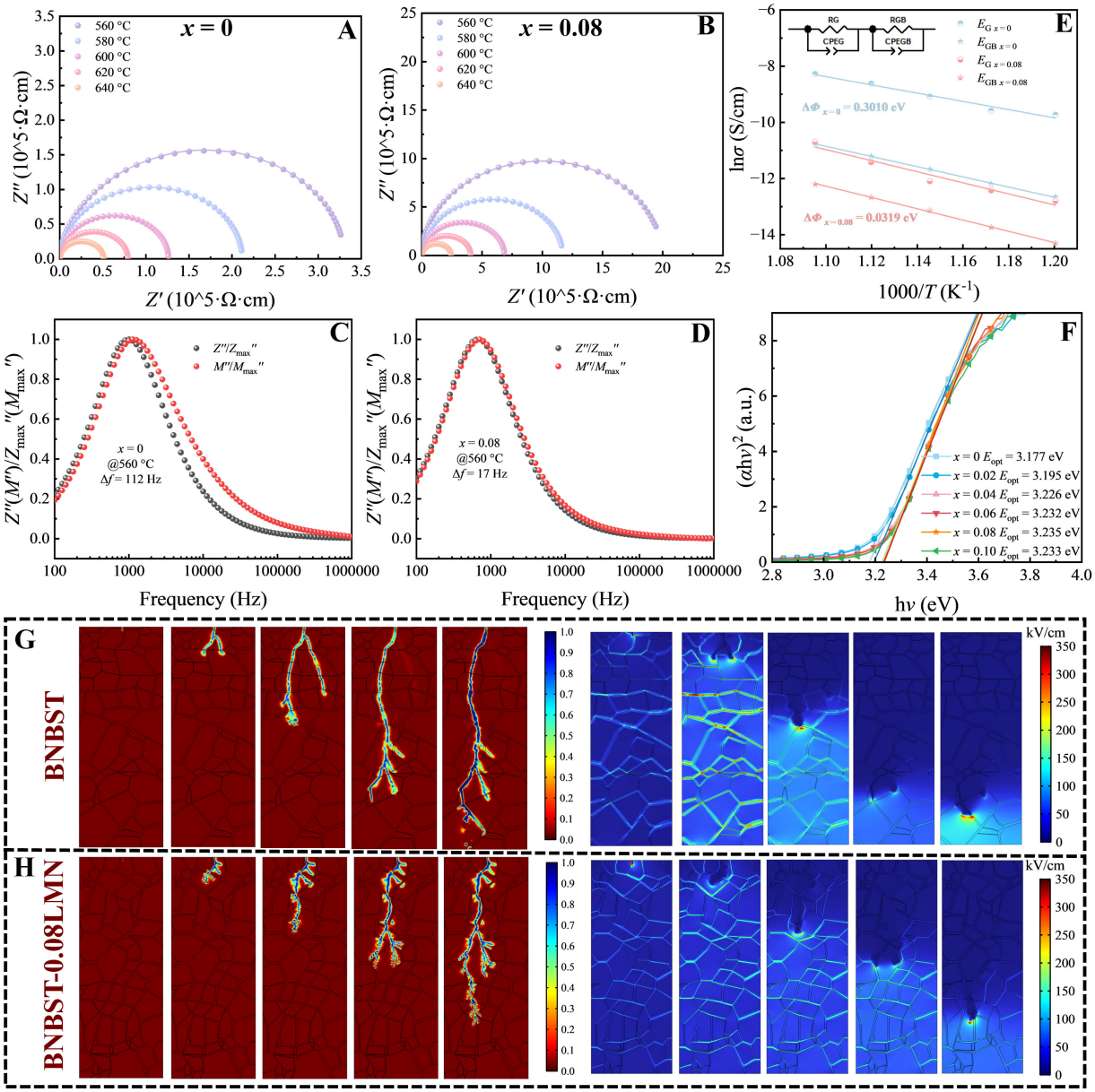


Figure 7. Temperature-dependent complex impedance spectra for the (A) x = 0 and (B) x = 0.08 ceramics. Frequency responses of the Z″ and M″ plots at 560 °C for the (C) x = 0 and (D) x = 0.08 ceramics. (E) Arrhenius plots of the grains and grain boundaries. (F) Tauc plots derived from the UV-Vis absorbance used to calculate E_{opt}. Finite-element simulation of the electric potential, local electric field, and electric tree propagation at 350 kV/cm for the (G) x = 0 and (H) x = 0.08 ceramics.

temperature-dependent impedance data to the Arrhenius equation ($\sigma = \sigma_0 \exp(-E_a/k_B T)$, where σ is the measured conductivity, σ_0 is a pre-exponential constant, E_a is the activation energy, k_B is the Boltzmann constant, and T is the absolute temperature). As shown in Figure 7E, pure BNBST demonstrates $\Delta\Phi$ = 0.3010 eV, reflecting pronounced heterogeneity, while BNBST-0.08LMN shows $\Delta\Phi$ = 0.0319 eV, which is an order of magnitude smaller and indicates a much more uniform electrical response. These results show that LMN modification simultaneously enhances the insulating properties of both grains and grain boundaries, leading to improved overall insulation and electrical homogeneity. The enhanced grain boundary insulation arises from the formation of a highly resistive Mg oxide compound at the grain boundaries, while the improved grain insulation is associated with the widening of the optical band gap (E_{gap}). To verify this, the E_{gap} value was extracted from UV-Vis absorbance data via Tauc plots based on the

Kubelka-Munk function [Figure 7F][56,60]. The E_{opt} values increase with increasing x value, and then converge when $x \geq 0.06$. Notably, the previous analysis suggests that Mg^{2+} ions enter the lattice when $x \leq 0.06$, thus increasing the E_{opt} value. At high x values, Mg^{2+} ions not only enter the lattice, but also form Mg oxide compounds at the grain boundaries, thereby resulting in a smaller variation in the E_{opt} value. In addition, the increased E_{opt} values increase the energy required for electron excitation, reducing the intrinsic carrier concentration and improving the insulating properties of the grains.

Finite-element simulations were conducted using realistic 2D microstructural models derived directly from the experimental SEM images to investigate the microscopic mechanisms governing dielectric breakdown and electric tree propagation. An electric field of 350 kV/cm was applied, and all relevant material parameters, including permittivity and conductivity, were carefully calibrated based on the dielectric and impedance properties. Figure 7G shows the time-resolved electrostatic potential and local electric field distributions obtained during tree initiation and growth in the pure BNBST ceramic. The simulation results clearly demonstrate that the permittivity contrast between high-permittivity grains and low-permittivity grain boundaries leads to a significant electric-field concentration at the grain boundaries. Due to the higher intrinsic breakdown strength of grain boundaries compared to grains, the electric trees initiate near the high-potential area and preferentially propagate through the weaker grain interiors. Notably, the BNBST-0.08LMN ceramic shows a slower electrical tree propagation than that of the pure BNBST ceramic [Figure 7H]. Moreover, the electric tree in the BNBST-0.08LMN ceramic displays a highly branched morphology with multiple bifurcations emerging around the main trunk, in contrast to the relatively simple tree shape observed in the pure BNBST ceramic. This behavior indicates that the retarded electric tree propagation arises not only from the smaller grain size and the larger fraction of grain boundaries, but also from the formation of multiple branching propagation paths that stem from the improved electrical homogeneity. These branched paths dissipate the electric-tree energy and force it to follow a more difficult route, significantly increasing the time to breakdown. Therefore, the superior insulation characteristics, combined with the multiply branched propagation routes, synergistically contribute to the enhanced E_b value of the BNBST-0.08LMN ceramic.

Energy storage performance stability and charging-discharging properties

The commercial viability of dielectric materials critically depends on their ability to maintain a consistent performance under the diverse and demanding conditions encountered in real-world applications. To comprehensively evaluate the operational stability and durability of the BNBST-0.08LMN ceramic, its unipolar *P-E* loops were assessed over a range of frequencies, temperatures, and fatigue cycles. The frequency dependence of the ESP, illustrated in Figures 8A and B, demonstrates good stability. Between 1 and 100 Hz, the *P-E* loops show negligible change, with η varying by less than 2%. This frequency insensitivity is highly desirable for applications requiring operation over a broad frequency spectrum. The temperature-dependent performance, presented in Figure 8C and D, shows that the BNBST-0.08LMN ceramic maintains a good ESP over a wide temperature range. From 20 to 160 °C, η stays within 7% of its room-temperature (20 °C) value, and W_{rec} slightly decreases. To investigate the microscopic origin of this slight W_{rec} reduction at high temperatures, *in situ* Raman spectroscopy measurements were performed from 20 to 200 °C [Figure 8E]. No new peaks appear as the temperature increases, indicating good structural stability at high temperatures. In addition, a gradual decrease in the peak intensities of the ν3, ν4, ν5, and ν6 modes at elevated temperatures is observed [Figure 8E1 and E2], which is due to the weakening of dipole correlations and smaller PNRs and hence slightly reduced P_{max} and W_{rec} values. Furthermore, the fatigue resistance of the BNBST-0.08LMN ceramic was evaluated by subjecting it to 10^5 unipolar polarization switching cycles [Figure 8F and G]. It also exhibits excellent fatigue resistance, with no significant degradation in the *P-E* loop shape and η varying by less than 3% even after 10^5 cycles. This good fatigue performance is attributed to the highly dynamic nature of the PNRs, which can easily switch their polarization direction without causing permanent damage to the

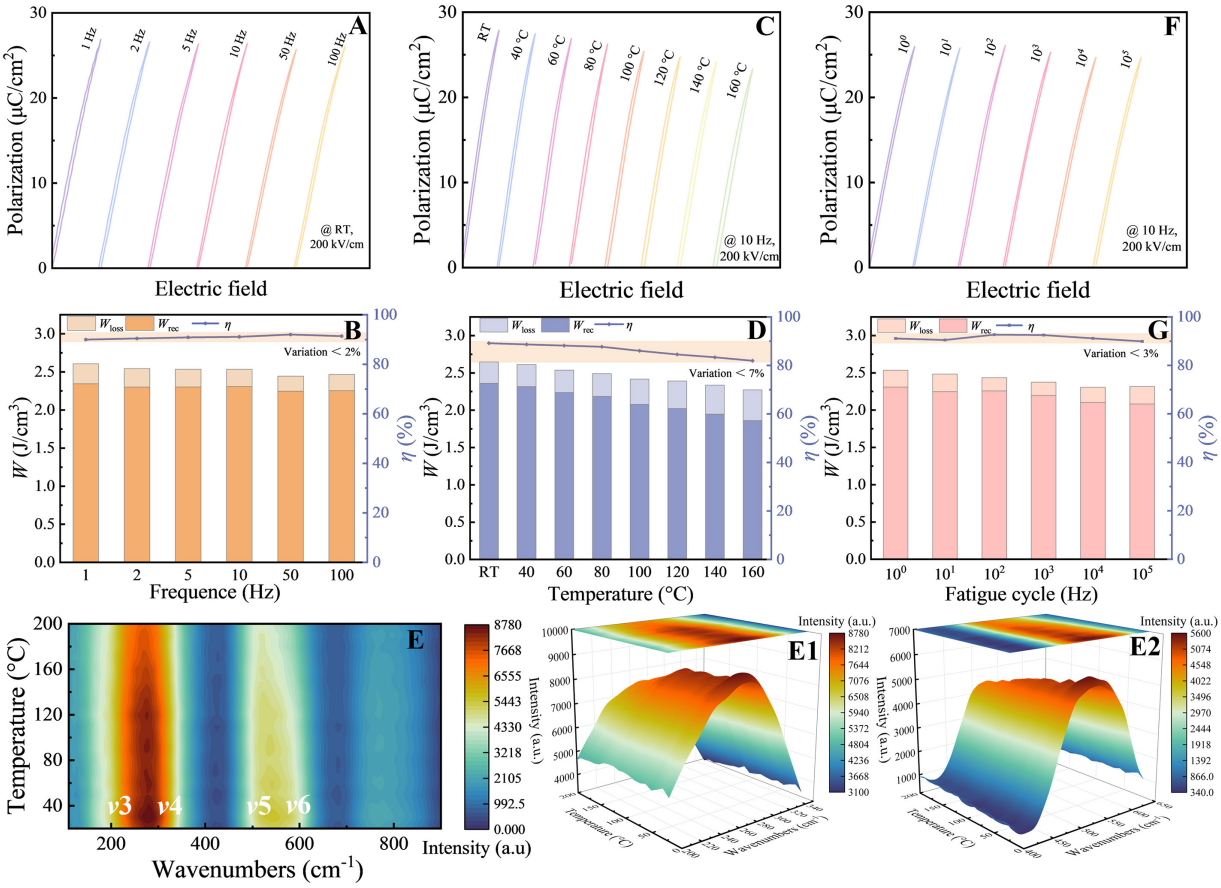


Figure 8. (A) Unipolar *P-E* loops measured at different frequencies from 1 to 100 Hz at room temperature (RT) (20 °C) and 200 kV/cm, and (B) the corresponding W_{rec}, W_{loss}, and η values. (C) Unipolar *P-E* loops measured from RT to 160 °C at 10 Hz and 200 kV/cm, and (D) the corresponding W_{rec}, W_{loss}, and η values. (E) Contour map of the *in situ* Raman spectra collected from 20 to 200 °C. Enlarged three-dimensional Raman intensity maps in the ranges of (E1) 200 to 350 cm^{-1} and (E2) 400 to 650 cm^{-1}. (F) Unipolar *P-E* loops measured after 1-10^5 fatigue cycles at 10 Hz and 200 kV/cm, and (G) the corresponding W_{rec}, W_{loss}, and η values.

material. Overall, the BNBST-0.08LMN ceramic combines a high ESP with stable operation over wide frequency, temperature, and cycling ranges, making it an attractive candidate for advanced dielectric energy-storage devices.

The ultimate test of any dielectric energy storage material is its performance under realistic operating conditions. To evaluate the practical charging-discharging properties of the BNBST-0.08LMN ceramic, we performed measurements in both overdamped and underdamped circuit conditions, which represent the two most common operating modes for pulsed power applications. In the overdamped circuit regime, which is typical for applications requiring controlled energy release, the two most important performance metrics are the discharge energy density (W_d) and the discharge rate ($t_{0.9}$). W_d was quantitatively determined by integrating the power dissipated across a 100 Ω load resistor using[61]

$$W_d = \frac{R\int I^2\,\mathrm{d}t}{V} \tag{13}$$

where R is the load resistance, V is the effective electrode volume, and I is the discharge current. The peak discharge current increases with the applied electric field and reaches its highest value at 240 kV/cm [Figure 9A], where W_d = 2.79 J/cm³ [Figure 9B]. The deviation of W_d from the theoretical recoverable energy

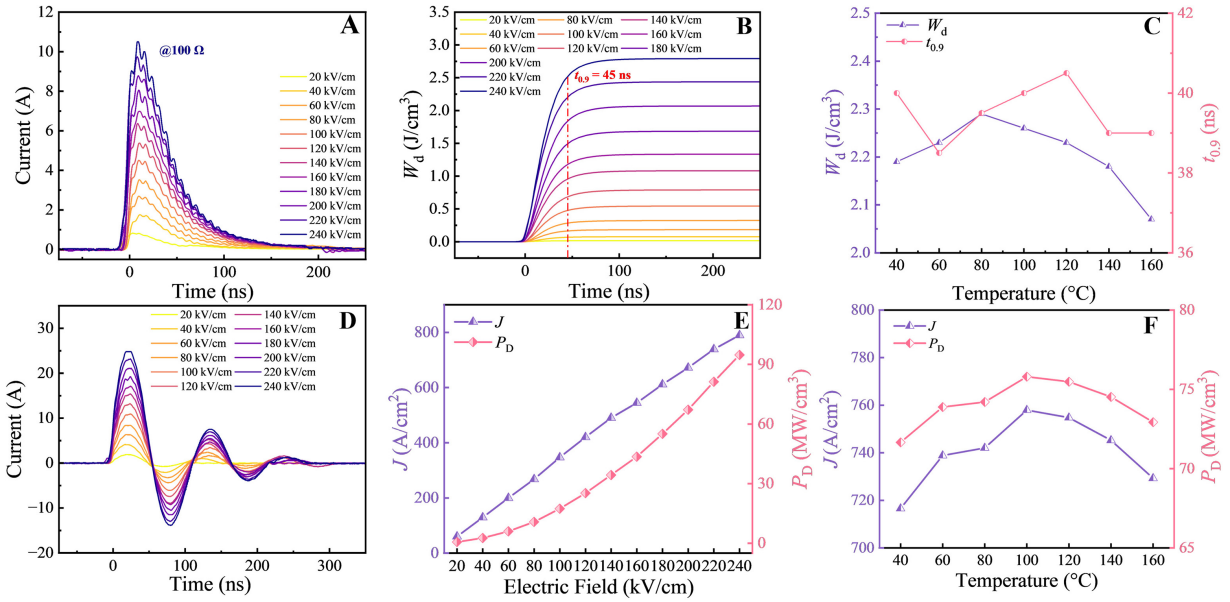


Figure 9. Charging-discharging properties under overdamped and underdamped circuit conditions. (A) Discharge curves under overdamped conditions and (B) the corresponding W_d values at different electric fields versus time. (C) Temperature dependence of W_d and $t_{0.9}$ at 200 kV/cm. (D) Discharge curves under underdamped conditions versus time and (E) the derived J and P_D values obtained at different electric fields. (F) Temperature evolution of J and P_D at 200 kV/cm.

density W_{rec} results from unavoidable energy losses originating from the external circuit load and the microstructural imperfections within the ceramic. Furthermore, the discharge rate, which is critical for pulsed power applications requiring rapid energy delivery, was characterized using the $t_{0.9}$ value, which is defined as the time required to release 90% of the total discharge energy. Notably, an ultrafast discharge rate is observed in the BNBST-0.08LMN ceramic, with $t_{0.9}$ remaining at approximately 45 ns over a wide electric field range. Moreover, the overdamped discharge performance stability was also investigated at 200 kV/cm over a wide temperature range [Supplementary Figure 7A and B, Figure 9C]. Within the tested temperature range, W_d shows only slight fluctuations between 2.07 and 2.29 J/cm³, and the discharge time remains below 40.5 ns, demonstrating the good thermal stability of the fast discharge properties.

In the underdamped circuit regime, the current density (J) and power density (P_D) are key performance indicators. These parameters were calculated using[62]:

$$J = \frac{I_{max}}{S} \tag{14}$$

$$P_D = \frac{E \times I_{max}}{2S} \tag{15}$$

where S and I_{max} are the electrode area and maximum current, respectively. Figure 9D shows the underdamped discharge curves as a function of the applied electric field. At 240 kV/cm, the BNBST-0.08LMN ceramic obtains J = 789.80 A/cm² and P_D = 94.77 MW/cm³ [Figure 9E]. The temperature-dependent curves measured at 200 kV/cm are shown in Supplementary Figure 7C. With increasing temperature, the discharge current exhibits more pronounced oscillatory behavior. At 100 °C, the J and P_D values reach maxima of 757.96 A/cm² and 75.79 MW/cm³, respectively [Figure 9F]. These results

demonstrate an exceptional charge-discharge performance in both circuit modes, positioning BNBST-0.08LMN as a strong candidate for advanced pulsed-power systems.

CONCLUSION

This paper presents a design strategy for lead-free BNBST-*x*LMN ceramics that achieve good ESP under moderate electric fields through HE and grain boundary engineering. The introduction of LMN increases the configurational entropy and induces phase competition, which widens the TCC. Phase-field simulation was used to quickly identify that the x = 0.08 model (S_{config} = 1.78 R) has a low P_r and high P_{max} under normalized electric fields. The local structure of the BNBST-0.08LMN ceramic exhibits the coexistence of short-range polar and long-range nonpolar regions, accompanied by randomly tilted oxygen octahedra, which enables fast and reversible polarization switching behavior while maintaining strong local dipole correlations. In addition, Mg oxide compounds are observed within the grain boundaries of the BNBST-0.08LMN ceramic, which act as pinning centers that refine the grain size and enhance the insulation performance. Moreover, improved insulation performance and more homogeneous electrical behavior between grains and grain boundaries slow the propagation of electric trees, enhancing breakdown strength. As a result, the BNBST-0.08LMN ceramic achieves W_{rec} = 6.50 J/cm^3 and η = 86.42% at 450 kV/cm; retains a stable ESP over 1-100 Hz, at 20-160 °C, and for up to 10^5 fatigue cycles; and exhibits a discharge time of only 45 ns. This work not only demonstrates the realization of a high-performance lead-free BNT-based ceramic for practical energy storage applications but also provides a general design method for achieving excellent ESP at moderate electric fields through HE and grain boundary engineering. Furthermore, the present study is limited to bulk ceramics; future work should extend this strategy to multilayer ceramic capacitors and evaluate their long-term operational reliability.

DECLARATIONS

Acknowledgments

We would like to thank the Jiangxi Key Laboratory of Advanced Ceramic Materials and the China National Light Industry Key Laboratory of Functional Ceramic Materials.

Authors' contributions

Conceptualization, data curation, formal analysis, funding acquisition, methodology, writing-original draft: Yu, C.

Formal analysis, funding acquisition, methodology: Li, D. X.

Data curation: Wang, Z.; Liu, W.; Zhang, Y.; Zhou, Q.; Xu, Z.; Qiu, R.

Conceptualization, formal analysis, funding acquisition, methodology, project administration, supervision, writing-review & editing: Shen, Z. Y.

Availability of data and materials

The data supporting the findings of this study are available within this Article and its Supplementary Materials. Further data are available from the corresponding author upon request.

AI and AI-assisted tools statement

Not applicable.

Financial support and sponsorship

This work was supported by the National Natural Science Foundation of China (52267002), the Natural Science Foundation of Jiangxi Province (20252BAC250040 and 20252BEJ730247), the Early-Career Young Scientists and Technologists Project of Jiangxi Province (20262BEJ730070), the Basic Research and Frontier Technology Projects of Jingdezhen (2025JCY002), and the Pioneer Research Program of Jiangxi Provincial Center for Interdisciplinary Studies in Future-oriented Materials.

Conflicts of interest

All authors declared that there are no conflicts of interest.

Ethical approval and consent to participate

Not applicable.

Consent for publication

Not applicable.

Copyright

© The Author(s) 2026.

Supplementary Materials

Supplementary Materials

REFERENCES

1. Zubairi, H.; Lu, Z.; Zhu, Y.; Reaney, I. M.; Wang, G. Current development, optimisation strategies and future perspectives for lead-free dielectric ceramics in high field and high energy density capacitors. *Chem. Soc. Rev.* **2024**, *53*, 10761-90. DOI PubMed
2. Zhang, M.; Lan, S.; Yang, B. B.; et al. Ultrahigh energy storage in high-entropy ceramic capacitors with polymorphic relaxor phase. *Science* **2024**, *384*, 185-9. DOI
3. Aramberri, H.; Fedorova, N. S.; Íñiguez, J. Ferroelectric/paraelectric superlattices for energy storage. *Sci. Adv.* **2022**, *8*, eabn4880. DOI PubMed PMC
4. Fan, X.; Wang, J.; Yuan, H.; Zheng, Z.; Zhang, J.; Zhu, K. Multi-scale synergic optimization strategy for dielectric energy storage ceramics. *J. Adv. Ceram.* **2023**, *12*, 649-80. DOI
5. Li, S.; Zhang, C.; Li, S.; Zhang, L.; Wu, H. Enhanced energy-storage performance with optimized thermally stable dielectric property in BNT-BST ceramics modified by KNN doping. *J. Adv. Dielect.* **2024**, *14*, 2440011. DOI
6. Peng, H.; Hu, T.; Liu, Z.; et al. Antiferroelectric-like high-entropy superparaelectric enables ultrahigh energy-storage in multilayer capacitors. *Adv. Mater.* **2026**, *38*, e73066. DOI
7. Zhang, L.; Jing, R.; Huang, Y.; et al. Ultra-weak polarization-strain coupling effect boosts capacitive energy storage. *Adv. Mater.* **2024**, *36*, 2406219. DOI
8. Yang, J.; Ge, G.; Chen, C.; Shen, B.; Zhai, J.; Chou, X. Field-induced strain engineering to optimize antiferroelectric ceramics in breakdown strength and energy storage performance. *Acta. Mater.* **2023**, *257*, 119186. DOI
9. Yang, Y.; Liu, Z.; Guo, K.; et al. Deciphering the relationships among phase boundary, domain structure, and excellent electrical properties of ternary $Bi_{0.5}Na_{0.5}TiO_3$-$Bi_{0.2}Sr_{0.7}TiO_3$-$NaNbO_3$ ferroelectrics. *Ceram. Int.* **2024**, *50*, 48174-82. DOI
10. Wang, H.; Wu, S.; Fu, B.; et al. Hierarchically polar structures induced superb energy storage properties for relaxor $Bi_{0.5}Na_{0.5}TiO_3$-based ceramics. *Chem. Eng. J.* **2023**, *471*, 144446. DOI
11. Yan, F.; Qi, X.; Qian, J.; et al. Boosting capacitive energy storage performance of bismuth sodium titanate-based lead-free ceramics under low electric field. *Chem. Eng. J.* **2025**, *516*, 164247. DOI
12. He, S.; Lou, K.; Han, B.; et al. Superior energy storage density and efficiency in antiferroelectric-like BNT-based ceramics via single-element phase engineering. *J. Adv. Ceram.* **2025**, *14*, 9221056. DOI
13. Pan, Y.; Zhang, Y.; Dong, Q.; et al. Entropy-driven multi-scale enhancement of energy storage performance in $(Bi_{0.5}Na_{0.5})_{0.5}Ba_{0.5}TiO_3$ ceramics. *J. Materiomics.* **2025**, *11*, 101055. DOI
14. Yin, J.; Zhang, Y.; Lv, X.; Wu, J. Ultrahigh energy-storage potential under low electric field in bismuth sodium titanate-based perovskite ferroelectrics. *J. Mater. Chem. A.* **2018**, *6*, 9823-32. DOI
15. Cilaveni, G.; Ashok, Kumar. K.; Raavi, S. S. K.; Subrahmanyam, C.; Asthana, S. Control over relaxor, piezo-photocatalytic and energy storage properties in $Na_{0.5}Bi_{0.5}TiO_3$ via processing methodologies. *J. Alloys. Compd.* **2019**, *798*, 540-52. DOI
16. Chen, M.; Yan, N.; Zhang, J.; et al. Curved-dislocation-engineered local polar texturing in core-shell $Ba_{0.5}Bi_{0.5}Ti_{0.5}Fe_{0.5}O_3$-$Ca_{0.7}La_{0.2}ZrO_3$ ceramics for high-capacitive energy storage. *Adv. Funct. Mater.* **2026**, *36*, e27868. DOI
17. Yu, H.; Hu, T.; Wang, H.; et al. Design of polymorphic heterogeneous shell in relaxor antiferroelectrics for ultrahigh capacitive energy storage. *Nat. Commun.* **2025**, *16*, 886. DOI PubMed PMC
18. Zhang, X.; Zhao, L.; Qiu, Y.; et al. Achieving comprehensive temperature-stable energy storage properties in core-shell $Na_{0.4}K_{0.1}Bi_{0.5}TiO_3$@($SrZrO_3$-$BiMg_{0.5}Sn_{0.5}O_3$)@$SiO_2$ ceramics via a multi-scale synergistic optimization. *Chem. Eng. J.* **2023**, *462*, 142251. DOI
19. Zhang, Y.; Zhang, X.; Zhang, P.; Zhang, Y.; Shi, P.; Yue, Z. Domain engineered lead-free $Bi_{0.5}Na_{0.5}TiO_3$-$Bi(Ni_{0.5}Hf_{0.5})O_3$ relaxor ferroelectric ceramics for energy storage with low electric field applications. *J. Energy. Storage.* **2024**, *84*, 110847. DOI

20. Xu, M.; Zeng, D.; Wang, X.; et al. Optimizing the energy storage performance of $NaNbO_3$ ceramics by rare-earth-based composite perovskite $Sm(Mg_{0.5}Zr_{0.5})O_3$ modification. *Microstructures* **2023**, *3*, 2023034. DOI
21. Shen, Y.; Wu, L.; Zhao, J.; et al. Constructing novel binary $Bi_{0.5}Na_{0.5}TiO_3$-based composite ceramics for excellent energy storage performances via defect engineering. *Chem. Eng. J.* **2022**, *439*, 135762. DOI
22. Nie, X.; Jing, R.; Zhang, L.; et al. Coupled phase-boundary engineering and defect control for ultrahigh electrostrain with low hysteresis in lead-free BNBT-based ceramics. *Acta. Mater.* **2026**, *313*, 122284. DOI
23. Xie, B.; Li, Z.; Luo, H.; et al. Constructing superrelaxor critical state towards giant energy storage in lead-free dielectric ceramics. *Nat. Commun.* **2026**, *17*, 1583. DOI PubMed PMC
24. Chen, L.; Wang, N.; Zhang, Z.; et al. Local diverse polarization optimized comprehensive energy-storage performance in lead-free superparaelectrics. *Adv. Mater.* **2022**, *34*, 2205787. DOI
25. Jing, R.; Zhang, L.; Yang, Y.; et al. Synergistic design strategies breaking the energy storage trade-off in lead-free dielectrics. *Adv. Mater.* **2026**, *38*, e74343. DOI
26. Li, D.; Zheng, Z.; Yang, B.; et al. Atomic-scale high-entropy design for superior capacitive energy storage performance in lead-free ceramics. *Adv. Mater.* **2025**, *37*, 2409639. DOI
27. Habib, M.; Wang, H.; Fang, W.; et al. High-entropy chemical composition design for ultrahigh capacitive energy storage. *Adv. Sci.* **2025**, *13*, e21163. DOI PubMed PMC
28. Shi, W.; Meng, M.; Zhang, L.; et al. High-entropy engineering of BNKT-based ceramics enables ultrastable dielectric energy storage. *Chem. Eng. J.* **2025**, *522*, 167352. DOI
29. Huang, Y.; Shang, K.; Yang, Y.; et al. Ultrahigh energy storage capacities in high-entropy relaxor ferroelectrics. *J. Mater. Chem. A.* **2024**, *12*, 18224-33. DOI
30. Zeng, X.; Lin, J.; Shen, J.; et al. Giant capacitive energy storage in high-entropy lead-free ceramics with temperature self-check. *Adv. Mater.* **2024**, *36*, 2409059. DOI
31. Zhang, Y.; Zhang, Z.; Bai, H.; et al. Advanced energy storage properties and multi-scale regulation mechanism in $(1-x)(Bi_{0.5}Na_{0.5})_{0.7}Sr_{0.3}TiO_3$-$xCa(Nb_{0.5}Al_{0.5})O_3$ relaxor ferroelectric ceramics. *Acta. Mater.* **2024**, *276*, 120109. DOI
32. Yang, Y.; Zhang, L.; Huang, Y.; et al. Entropy-driven polarization disordering enables ultrahigh energy storage performance in lead-free ferroelectric ceramics. *Adv. Funct. Mater.* **2026**, *36*, e76402. DOI
33. Meng, X.; Yuan, Y.; Wang, H.; Tang, B.; Li, E. Superior energy-storage performances under a moderate electric field achieved in antiferroelectric-like $Na_{0.5}Bi_{0.5}TiO_3$-based relaxor ferroelectric ceramics by a synergistic optimization strategy. *ACS. Appl. Mater. Interfaces.* **2024**, *16*, 67979-94. DOI
34. Cao, W.; Li, L.; Zhao, H.; et al. Outstanding energy storage performance of NBT-based ceramics under moderate electric field achieved via antiferroelectric engineering. *ACS. Appl. Mater. Interfaces.* **2023**, *15*, 38633-43. DOI
35. Zeng, X.; Lin, J.; Chen, Y.; et al. Superior energy storage capability and fluorescence negative thermal expansion of $NaNbO_3$-based transparent ceramics by synergistic optimization. *Small* **2024**, *20*, 2309992. DOI
36. Ning, Y.; Pu, Y.; Wu, C.; et al. Enhanced capacitive energy storage and dielectric temperature stability of A-site disordered high-entropy perovskite oxides. *J. Mater. Sci. Technol.* **2023**, *145*, 66-73. DOI
37. Zhang, X.; Zhang, F.; Niu, Y.; Zhang, Z.; Bai, Y.; Wang, Z. Effect of La substitution on energy storage properties of $(Bi_{0.2}Na_{0.2}Ca_{0.2}Ba_{0.2}Sr_{0.2})TiO_3$ lead-free high-entropy ceramics. *J. Am. Ceram. Soc.* **2023**, *106*, 6641-53. DOI
38. Tao, Y.; Yang, H.; Wang, M.; Zheng, B.; Lin, Y. High energy storage efficiency and exceptional recoverable energy storage density achieved in KNN-based ceramics via entropy engineering. *J. Alloys. Compd.* **2025**, *1024*, 180210. DOI
39. Yang, H.; Qi, H.; Zuo, R. Enhanced breakdown strength and energy storage density in a new $BiFeO_3$-based ternary lead-free relaxor ferroelectric ceramic. *J. Eur. Ceram. Soc.* **2019**, *39*, 2673-9. DOI
40. Su, Q.; Ma, Z.; Zhu, J.; et al. Excellent energy-storage performance in BNT-SST-LMN lead-free relaxor ferroelectric ceramics with high electrical homogeneity. *ACS. Appl. Energy. Mater.* **2022**, *5*, 15247-56. DOI
41. Cao, M.; Zhang, X.; Yang, S.; et al. Realizing high energy storage performance in $(Bi_{0.5}Na_{0.5})_{0.7}Sr_{0.3}TiO_3$ ceramics*via* phase structure adjustment. *J. Mater. Chem. A.* **2025**, *13*, 14181-8. DOI
42. Malasi, A.; Nanda, N.; Swain, S.; Kumar, P. Tailoring breakdown behaviour in BST-*x*MgO ceramics for energy storage applications. *J. Alloys. Compd.* **2025**, *1038*, 182737. DOI
43. Che, R.; Yang, K.; You, W.; Cen, Z.; Luo, N. Excellent energy storage performance in $Bi_{0.5}Na_{0.5}TiO_3$ high-entropy relaxor ferroelectrics modified with multiple aliovalent B-site ions. *Microstructures* **2026**, *6*, 2026013. DOI
44. Sun, Z.; Luo, T.; Gao, P.; et al. Machine-learning-designed BCZT-SBT heterointerface unlocks fatigue-resistant energy storage. *Adv. Mater.* **2025**, *38*, e19635. DOI

45. Sun, Z.; Li, Y.; Yang, H.; et al. Machine-learning-guided polarization-lattice decoupling enables ultrahigh energy storage in lead-free dielectric ceramics. *Adv. Mater.* **2026**, e73801. DOI
46. Sun, Z.; Diwu, L.; Gao, R.; et al. Machine learning-driven ultra-high energy storage performance in ferro-superparaelectric capacitors. *Adv. Funct. Mater.* **2025**, *36*, e16412. DOI
47. Li, D.; Shen, Z.; Li, Z.; et al. Structural evolution, dielectric and ferroelectric properties of (1-*x*)$Bi_{0.5}Na_{0.5}TiO_3$-*x*$Ba_{0.3}Sr_{0.7}TiO_3$ ceramics. *J. Mater. Sci. Mater. Electron.* **2019**, *30*, 5917-22. DOI
48. Li, Z.; Li, D.; Shen, Z.; et al. Remarkably enhanced dielectric stability and energy storage properties in BNT-BST relaxor ceramics by A-site defect engineering for pulsed power applications. *J. Adv. Ceram.* **2022**, *11*, 283-94. DOI
49. Chen, L.; Hu, T.; Shi, X.; et al. Near-zero energy consumption capacitors by controlling inhomogeneous polarization configuration. *Adv. Mater.* **2024**, *36*, 2313285. DOI
50. Shannon, R. D. Revised effective ionic radii and systematic studies of interatomic distances in halides and chalcogenides. *Acta. Cryst. A.* **1976**, *32*, 751-67. DOI
51. Reaney, I. M.; Enrico, L. Colla ELC, Nava Setter NS. Dielectric and structural characteristics of Ba- and Sr-based complex perovskites as a function of tolerance factor. *Jpn. J. Appl. Phys.* **1994**, *33*, 3984. DOI
52. Jones, G. O.; Thomas, P. A. Investigation of the structure and phase transitions in the novel A-site substituted distorted perovskite compound $Na_{0.5}Bi_{0.5}TiO_3$. *Acta. Cryst. B. Struct. Sci.* **2002**, *58*, 168-78. DOI
53. Petzelt, J.; Kamba, S.; Fábry, J.; et al. Infrared, Raman and high-frequency dielectric spectroscopy and the phase transitions in $Na_{1/2}Bi_{1/2}TiO_3$. *J. Phys. Condens. Matter.* **2004**, *16*, 2719-31. DOI
54. Zhao, H.; Cao, W.; Liang, C.; Wang, C.; Wang, C.; Cheng, Z. High-entropy design toward ultrahigh energy storage density under moderate electric field in bulk lead-free ceramics. *Adv. Funct. Mater.* **2024**, *35*, 2411954. DOI
55. Jia, W.; Hou, Y.; Zheng, M.; et al. Advances in lead-free high-temperature dielectric materials for ceramic capacitor application. *IET. Nanodielectrics.* **2018**, *1*, 3-16. DOI
56. Khokhar, A.; Narwal, A.; Yadav, K. L. Dynamic behavior of polar nano regions: enhanced energy density in the low electric field region via hybrid polarization mechanism in BNT-based relaxors. *Chem. Eng. J.* **2025**, *515*, 163751. DOI
57. Zhang, J.; Pu, Y.; Hao, Y.; et al. Novel ternary $BiFeO_3$-based perovskite-pyrochlore composite ceramics for enhanced energy-storage performance. *Chem. Eng. J.* **2025**, *516*, 164008. DOI
58. Wang, X.; Huan, Y.; Zhao, P.; et al. Optimizing the grain size and grain boundary morphology of (K,Na)NbO_3-based ceramics: paving the way for ultrahigh energy storage capacitors. *J. Materiomics.* **2021**, *7*, 780-9. DOI
59. Wu, C.; Qiu, X.; Chen, L.; et al. A strategy to achieve high energy storage performance under a relatively low electric field in NBT-based ceramics. *J. Alloys. Compd.* **2022**, *910*, 164851. DOI
60. Zhang, X.; Zhao, L.; Liu, L.; Zhang, Z.; Cui, B. Interface and defect modulation via a core-shell design in ($Na_{0.5}Bi_{0.5}TiO_3$@La_2O_3)-($SrSn_{0.2}Ti_{0.8}O_3$@La_2O_3)-Bi_2O_3-B_2O_3-SiO_2 composite ceramics for wide-temperature energy storage capacitors. *Chem. Eng. J.* **2022**, *435*, 135061. DOI
61. He, B.; Zhou, B.; Yan, S.; Cao, F.; Chen, X.; Wang, G. Ultrahigh energy density and efficiency $BaTiO_3$-based multilayer ceramic capacitors. *J. Adv. Ceram.* **2025**, *14*, 9221018. DOI
62. Dan, Y.; Tang, L.; Ning, W.; et al. Achieving enhanced energy storage performance and ultra-fast discharge time in tungsten-bronze ceramic. *J. Adv. Ceram.* **2024**, *13*, 1349-58. DOI

Disclaimer/Publisher's Note: All statements, opinions, and data contained in this publication are solely those of the individual author(s) and contributor(s) and do not necessarily reflect those of OAE and/or the editor(s). OAE and/or the editor(s) disclaim any responsibility for harm to persons or property resulting from the use of any ideas, methods, instructions, or products mentioned in the content.

© The Author(s) 2026. Open Access This article is licensed under a Creative Commons Attribution 4.0 International License (https://creativecommons.org/licenses/by/4.0/), which permits unrestricted use, sharing, adaptation, distribution and reproduction in any medium or format, for any purpose, even commercially, as long as you give appropriate credit to the original author(s) and the source, provide a link to the Creative Commons license, and indicate if changes were made.